CO2-induced switching between MOF-based bio-mimic slow anion channel and proton pump for medical exhalation detection

Chen, Honghao; Yue, Xiaorui; Fan, Yifei; Zheng, Bin; Lv, Sitao; Wang, Fengnan; Gao, Yixun; French, Patrick J.; Wang, Yao; More Authors

DOI
10.1016/j.cej.2024.152633

Publication date
2024

Document Version
Final published version

Published in
Chemical Engineering Journal

Chemical Engineering Journal 493 (2024) 152633

Contents lists available at ScienceDirect

Chemical Engineering Journal

journal homepage: www.elsevier.com/locate/cej

CO_2-induced switching between MOF-based bio-mimic slow anion channel and proton pump for medical exhalation detection

Honghao Chen [a,b], Xiaorui Yue [a,b], Yifei Fan [a,b], Bin Zheng [a,b], Sitao Lv [a,b], Fengnan Wang [c], Yixun Gao [a,b], Hao Li [a,b], Yi-Kuen Lee [d,e], Patrick J. French [f], Ahmad M. Umar Siddiqui [g], Yao Wang [a,b,1,*], Guofu Zhou [a,b]

[a] *Guangdong Provincial Key Laboratory of Optical Information Materials and Technology & Institute of Electronic Paper Displays, South China Academy of Advanced Optoelectronics, South China Normal University, Guangzhou 510006, PR China*
[b] *National Center for International Research on Green Optoelectronics, South China Normal University, Guangzhou 510006, PR China*
[c] *Department of Thoracic Oncology State Key Laboratory of Respiratory Diseases, The First Affiliated Hospital of Guangzhou Medical University, Guangzhou 510006, PR China*
[d] *Department of Mechanical & Aerospace Engineering, Hong Kong University of Science and Technology, Clear Water Bay, Kowloon, Hong Kong Special Administrative Region, PR China*
[e] *Department of Electronic & Computer Engineering, Hong Kong University of Science and Technology, Clear Water Bay, Kowloon, Hong Kong Special Administrative Region, PR China*
[f] *BE Lab, Faculty EWI, Delft University of Technology, Delft 2628CD, The Netherland*
[g] *Department of chemistry, Faculty of Science and Arts and Promising Centre for Sensors and Electronic Devices (PCSED), Najran University, Najran, 11001, Saudi Arabia*

ARTICLE INFO

Keywords:
Carbon dioxide
Chemiresistive gas sensor
γ-cyclodextrin-MOF
Dual ion channel
Hydrogen bond
Exhalation detection

ABSTRACT

Inspired by the activation mechanism of slow anion channels 1 (SLAC1) in plants that proton pump reversibly induces plant stomata open for CO_2 adsorption, a CO_2-switching H+ conduction/HCO_3^- diffusion dual ion channel (CO_2-switching-DIC) was constructed by assembling γ-cyclodextrin-MOF (γ-CD-MOF) and 3,4,9,10-perylenetetracarboxylic acid (PTCA) for CO_2 chemiresistive sensing. The obtained CO_2 sensor exhibited high response (R_g/R_0 = 1.33, 50 ppm) and selectivity, low practical limit of detection (1 ppm) and excellent consistency (94.5%) with a commercial infrared CO_2 meter at room temperature. It is indicated that hydrogen bond networks in CO_2-switching-DIC will be enlarged with the increasing of carboxylic group's content on perylene skeleton, thereby modulating proton conductivity at molecular level and furthermore CO_2 sensing performance of the composite. The CO_2-switching-DIC-based sensor has been utilized to distinguish the exhaled CO_2 concentration between lung cancer patients and healthy individuals, illustrating its promising application prospect in non-invasive diagnose.

1. Introduction

In nature, Carbon dioxide (CO_2) is one of the most abundant and important gases, a gaseous substance on which plants and animals depend for their survival [1–3]. In humans, in addition to its well-known role as a greenhouse gas, CO_2 is increasingly recognized as an important physiological exhaled gas that can provide information about physical health [4–6]. For example, testing for changes in exhaled CO_2 concentration due to exercise and disease can be used to assess physical health [7]. Recent studies have shown that CALU-1 lung cancer cells produce more CO_2 than normal lung epithelial cells NL20 [8], which means that concentration of exhaled CO_2 could be a non-invasive protocol for lung cancer diagnosis.

Compared to common diagnostic techniques such as computed tomography (CT), positron emission tomography (PET), low-dose CT (LDCT) and radiography those are unfriendly to universal community because they have high false-positive rates, bulky equipment and operational complexities [9–11], using portable, easy-to-use and non-

* Corresponding author at: Guangdong Provincial Key Laboratory of Optical Information Materials and Technology & Institute of Electronic Paper Displays, South China Academy of Advanced Optoelectronics, South China Normal University, Guangzhou 510006, PR China.
E-mail address: wangyao@m.scnu.edu.cn (Y. Wang).
[1] 0000–0002–0713–5018.

https://doi.org/10.1016/j.cej.2024.152633
Received 12 March 2024; Received in revised form 30 April 2024; Accepted 27 May 2024
Available online 1 June 2024

invasive gas-sensor technology for exhaled CO_2 detection not only saves the cost of testing, but also improves convenience and reduces the discomfort of the diagnostic process.

At present, commercial CO_2 sensor technologies are dominated by infrared spectroscopy [12,13], gas chromatography [14] and photoacoustic spectroscopy [15]. Although these methods are sensitive and selective, they have equipment requirements and are not conducive to real-time, field-based exhaled breath testing, especially for community-based medical care outside city. In contrast, chemiresistive CO_2 sensors have attracted more attention owing to their microfabrication potential, low cost, and convenience of operation. As we know, the sensing material essentially determines the actual performance of chemiresistive sensors. Traditional chemiresistive CO_2 sensing materials are mainly metal oxide semiconductors (MOS) such as CeO_2, In_2O_3 etc., and often require high operation temperature (>100 °C) [16,17], which not only causes an unnecessary safety risk and high energy consumption, but also has poor selectivity toward CO_2. Therefore, there is an urgent demand to develop a low energy consumption, high-sensitivity and selectivity chemiresistive CO_2 sensing material.

As a new material with ordered nanostructure, metal–organic frameworks (MOFs) are ideal candidates for chemiresistive CO_2 sensing materials owing to their large-surface-area, stable and porous nanostructure [18,19]. The CO_2 sensing mechanisms of MOF-based materials mainly include Lewis acid-base reaction, oxidation reaction, breathing effect of MOF and ionic conduction [20–26], but all of them still face the challenges including high practical limit of detection (pLOD), low sensitivity and high energy consumption for their practical applications. In 2010, Stoddart et al. at Northwestern University alternatively reported an ion-conducting CD-MOF-2 for electrochemical sensing of high concentrations of CO_2 (>100,000 ppm). High concentrations of CO_2 interacted with the hydroxyl group of CD-MOF-2, whose β-window was blocked, resulting in decreased proton conductivity. Unfortunately, due to its intrinsic structure, this material is not able to work for detecting low concentration CO_2 (<100,000 ppm). Then, seeking another effective way for CD-MOF to detect low concentration CO_2 in exhalation detection is demanded [27,28].

In nature, activation of the plasma membrane (PM) H^+-ATPase allows the proton pump to be turned on in plants. In this process, the extrusion of H^+ leads to a decrease in pH, which favors the opening of stomatal apertures and results in the activation of the slow anion channel 1 (SLAC1) via the uptake of CO_2 molecules [29–34]. Inspired by this process, we envisioned whether we could develop an artificial ion channel simulating this CO_2 sensing mechanism: (i) constructing an artificial H^+ conduction channel with mechanism mimicking natural H^+-ATPase activated H^+ extrusion in plants (Fig. 1b). (ii) constructing an artificial anion conduction channel with mechanism mimicking natural CO_2-induced reversible activation of SLAC1 in plants (Fig. 1d). In our previous work, a bio-inspired γ-CD-MOF-derived CO_2-switching proton/hydroxide ion channel (CSPH ion channel) has been developed for low concentration CO_2 sensing (<100,000 ppm) and its validity has preliminary been verified in distinguishing the exhaled CO_2 between the healthy and the recovered COVID-19 patients [35]. It has been proved that γ-CD-MOF can serve as a proton pump-mimic carrier to load carboxyl-contained small molecules. Based on the above exploration, we would further investigate more applications in disease diagnosis via exhalation detection using γ-CD-MOF based ion channels. Herein, 3,4,9,10-perylenetetracarboxylic acid (PTCA) was selected as a multi-carboxyl proton producer, providing content-adjustable protons for the formation of expected hydrogen bond network (Fig. 1a). In this case, the slight interference of hydrogen bond network caused by low concentration CO_2 could be exhibited by the little change in proton conductivity of the composite (Fig. 1c).

In details, we loaded PTCA into γ-CD-MOF to construct a CO_2-switched H^+ conduction/HCO_3^- diffusion dual ion channel (CO_2-switching-DIC) through supramolecular interaction. This CO_2-switching-DIC was then integrated into an Ag/Pt interdigitated electrode to build a sensor for room temperature exhaled CO_2 detecting (Fig. 1). The carboxyl of PTCA can form hydrogen bonds with hydroxyl ions, which would expand the structure of hydrogen bond network and is expected to greatly enhance the proton conductivity of the composite for CO_2 sensing. More importantly, expanding the hydrogen bond network by adjusting the carboxyl content of perylene can regulate proton conductivity at molecular level, improving the sensitivity of the obtained CO_2 sensor.

2. Experimental section

2.1. Preparation of γ-CD-MOF, γ-CD-MOF@PTCA, γ-CD-MOF@PDCA and γ-CD-MOF@PCA

γ-cyclodextrin (99%) and 3-perylcarboxylic acid (PCA, 98%) were purchased from Inno-chem. 3,4,9,10-perylenetetracarboxylic acid (PTCA, 98%) 3,9-perylenedicarboxylic acid (PDCA, 98%) from Bide. Potassium hydroxide (KOH, 99%) was purchased from Sigma-Aldrich. The preparation method used in this paper was modified from that previously reported in the literature [18–20]. Firstly, appropriate amounts of cyclodextrins and potassium hydroxide (molar ratio 1:10) were placed into a 20 mL glass vial containing 5 mL of deionized water, sonicated vigorously for 30 min, and then filtered through 0.45 μm nylon filter membrane. The glass vial was sealed in a blue-capped glass bottle containing 20 mL of methanol and vaporized for 10 days to obtain γ-CD-MOF solid particles. Then the mother liquor was filtered out and washed with methanol for three times, and then dried under vacuum at 60 °C. The obtained solid particles were then used for characterization.

For γ-CD-MOF@PTCA and γ-CD-MOF@PDCA and γ-CD-MOF@PCA, the co-crystallization method was adopted. Initially, an appropriate quantity of γ-cyclodextrin and potassium hydroxide (in a molar ratio of 1:10) was added to a 20 mL glass vial containing 5 mL of deionized water. Subsequently, a specific proportion of PTCA, PDCA or PCA was then added, and the undissolved impurities were filtered through a 0.45 μm filter membrane after sonication for 30 min. The glass vials were then sealed in a blue-capped glass bottle containing 20 mL of methanol and vaporized for 10 days to obtain γ-CD-MOF@PTCA, γ-CD-MOF@PDCA or γ-CD-MOF@PCA solid particles. The mother liquor was then filtered out using a nylon filter membrane, washed three times with methanol and dried in vacuum at 60 °C. The solid particles were then used for characterization.

2.2. Sensor preparation and gas-sensitive performance measurements

The preparation process of the CO_2 sensor was similar to our previous report [35]. Briefly, 10 μL of the sensing material dispersion (0.1 mg/μL) was drop-coated onto an interdigital electrode (IDE), which was then dried at 50 °C for 15 min. The IDE was then connected to a Keithley 2450 signal source meter (Tektronix, USA) via a wire and the change in resistance of the prepared sensor was recorded. A 1,000, 000 ppm of dry CO_2 standard gas was purchased from Dalian Specialty Gases Company. A humidity-controlled dynamic gas distribution system (DGL-III, Elite Technology Co., Ltd., China) was used to configure the background gas at a certain humidity level (5–70% RH, N_2) in a 1 L sealed test chamber. All measurements were performed at room temperature (26 ± 2 °C). Throughout the experiment, the IDE housing the sensing material was positioned within a hermetically sealed testing chamber, which was maintained at a nitrogen atmosphere with controlled humidity levels. After the baseline was stabilized, different volumes of dry CO_2 were injected and the change in resistance of the sensor at different concentrations of CO_2 was recorded. Then, the IDE was placed in another test chamber containing nitrogen gas of the same humidity for response. Here, the response value is defined as $R = R_g/R_0$, where R_g is the resistance value after injection of the target gas and R_0 is the resistance value at baseline. Response time and recovery time are defined as the time at which the response and recovery are fully 90%, respectively.

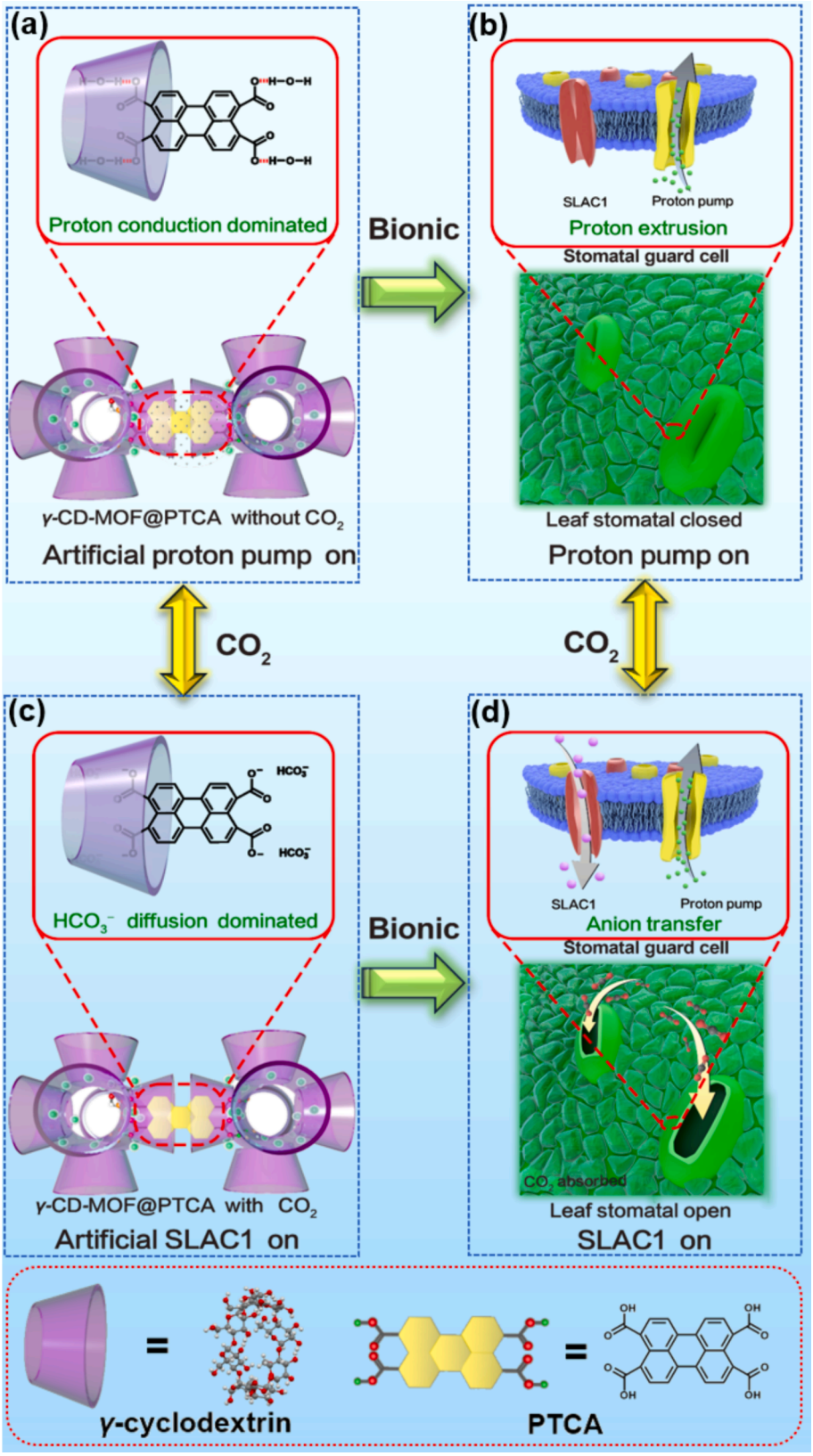

Fig. 1. Schematic diagram of the proposed CO_2-switching-DIC sensing material. (a) Hydrogen bond network of γ-CD-MOF@PTCA. (b) Schematic diagram of the proton pump in leaf stomatal guard cells. (c) HCO_3^- diffusion process in γ-CD-MOF@PTCA. (d) Schematic diagram of proton pump-induced CO_2 adsorption and subsequent reversible activation of SLAC1. (Purple balls: anions such as NO_3^-, Cl^-. Green balls: hydrogen ions.). (For interpretation of the references to color in this figure legend, the reader is referred to the web version of this article.)

2.3. Characterization of materials

A powder diffraction X-ray instrument (XRD, D8 Advance, Bruker, Germany) was used to characterize the crystal structure of the prepared materials using Cu as incident radiation. Fourier transform infrared spectrophotometer (FT-IR, Vertex 70, Bruker, Germany) was used to characterize the chemical groups of the materials. Fluorescence spectroscopy (PL, RF-6000, Shimadzu, Japan) was used to measure the content of fluorophores (PTCA, PDCA, PCA). Elemental content was determined by X-ray photoelectron spectroscopy (XPS, AXIS Supra, Shimadzu, Japan). The morphology of the prepared samples was analyzed by field emission electron scanning microscopy (FESEM, Carl Zeiss ZEISS Ultra 55, Germany). The morphology and X-ray energy dispersive spectroscopy (EDS) of the prepared samples were analyzed by field emission transmission electron microscopy (FETEM, FEI Talos F200X, USA). The samples were pretreated for 12 h under vacuum at 50 °C using the standard degassing station on the instrument, and then the samples were subjected to nitrogen adsorption–desorption test using a fully automated Specific Surface Area Analyzer of the Autosorb-IQ-MP, Quantachrome of the U.S.A. under the condition of 77 K. The nitrogen adsorption–desorption isothermal curves were obtained when the instrument had finished analyzing the samples to obtain the total specific surface area of the materials by the BET method.

2.4. Measurement of proton conductivity (σ) of MOF films

The proton conductivity of the material was measured by electrochemical impedance spectroscopy. Briefly, γ-CD-MOF@PTCA solids were ground into powder and then pressed into circular sheets. The diameter and thickness of the circular flakes were measured using digital calipers (diameter d = 12.60 mm and thickness l = 0.59 mm). Then, both sides of the circular flake were connected to the electrodes of an electrochemical impedance spectrometer and placed in a thermostat. The impedance spectroscopy test conditions were 0.01 Hz–1 MHz with an amplitude voltage of 0.025 V and a test temperature of 30–60 °C.

2.5. Detection of human exhaled gas

Human exhaled gas was first collected in a 1 L aluminum foil gas collection bag. To avoid the influence of humidity, the exhaled gas was injected into a drying device equipped with blue silica gel (38 mm × 25 mm, Yuxin, China) before measurement, and the saturation of the water-absorbing capacity of the silica gel was confirmed by observing the color, and the dehumidifying effect of the drying device was confirmed by measuring the humidity of the gas. Then, CO_2 measurement was performed with the dried exhaled gas. Commercial IR meter purchased from Hengxin, Taiwan, China, with a CO_2 detection range of 0–9999 ppm and a detection error of ± 50 ppm.

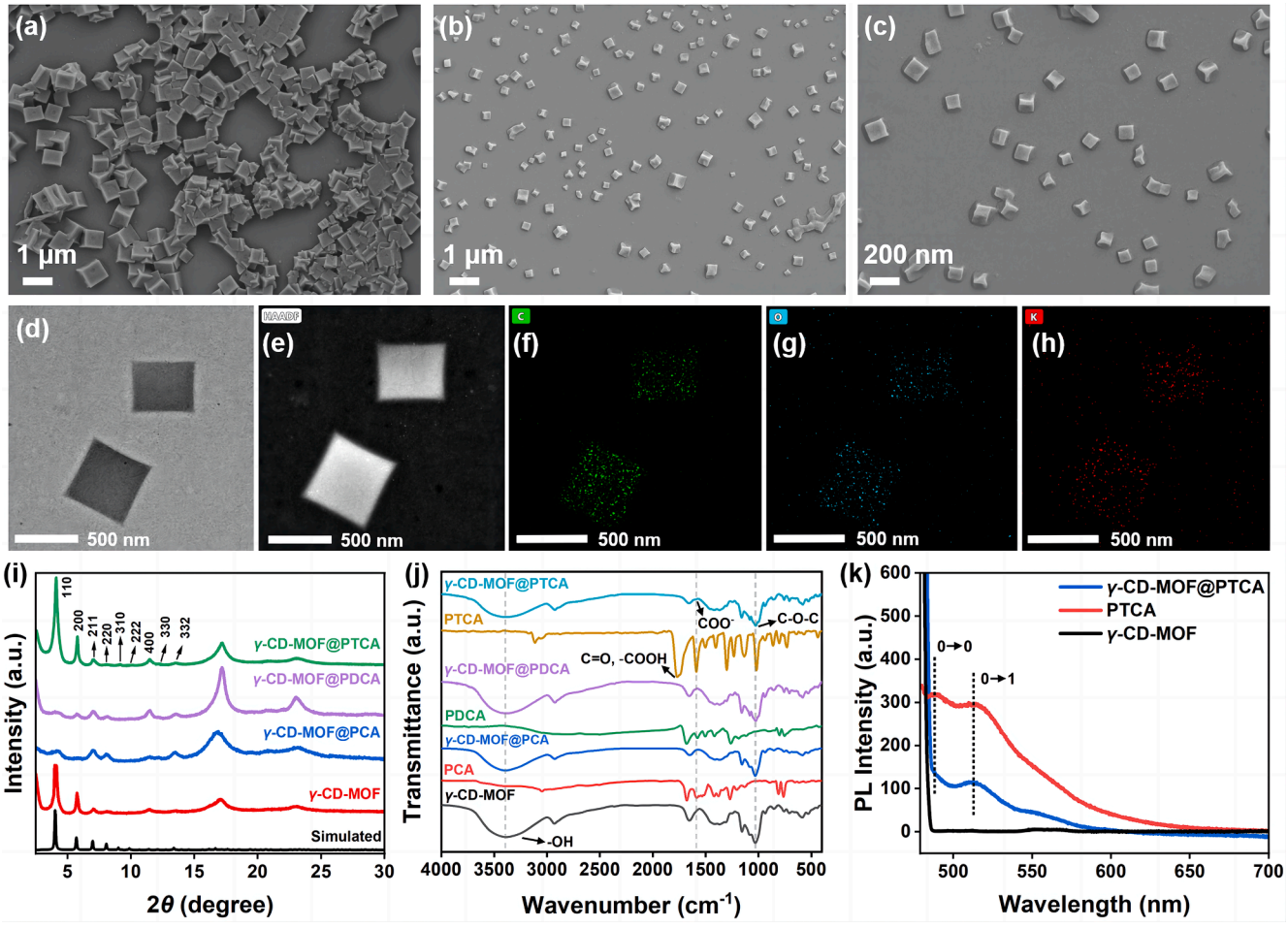

Fig. 2. Characterization of gas-sensing materials. SEM images of (a) γ-CD-MOF and (b–c) γ-CD-MOF@PTCA. (d) TEM images and (e) HAADF-STEM images of γ-CD-MOF@PTCA. EDS mapping images of TEM of (f) C, (g) O, (h) K of γ-CD-MOF@PTCA. (i) Powder X-ray diffraction pattern (PXRD) of γ-CD-MOF, γ-CD-MOF@PCA, γ-CD-MOF@PDCA and γ-CD-MOF@PTCA. (j) Fourier transform infrared spectroscopy (FT-IR) of γ-CD-MOF, PCA, γ-CD-MOF@PCA, PDCA, γ-CD-MOF@PDCA, PTCA and γ-CD-MOF@PTCA. (k) Fluorescence spectra of γ-CD-MOF@PTCA, γ-CD-MOF and PTCA.

3. Results and discussion

3.1. Structure and characterization

It is known that the cavity size of γ-CD is 9.5 Å, which can be more compatible with the width of PTCA molecule (around 7 Å) [36–38]. In addition, it is possible to encapsulate the small molecule only in the γ-CD cavity of γ-CD-MOF by the co-crystallization method [39,40]. Inspired by this, PTCA, PDCA, and PCA were encapsulated into γ-CD-MOF by co-crystallization method (Fig. S1a). Then, the obtained solid nanoparticles were dispersed in methanol solution and drop-coated onto an interdigital electrode (IDE) for CO_2 gas sensing (Fig. S1b).

As shown in Fig. 2a, scanning electron microscopy (SEM) demonstrated the cubic structure of γ-CD-MOF, which is in agreement with that previously reported [27,28]. Although γ-CD-MOF@PTCA also maintains a cubic structure, its size is smaller (less than 1 μm) compared to γ-CD-MOF, which is attributed to the fact that the loading of PTCA induces a competitive coordination reaction between K^+ ions and carboxylate groups, resulting in the smaller size of γ-CD-MOF@PTCA due to the limited coordination of γ-CD and K^+. On the other hand, the smaller size means that it has a larger specific surface area, which is favourable for the diffusion of the target gas (Fig. 2b–c). Fig. 2d and e show transmission electron microscopy (TEM) and high-angle annular dark field scanning transmission electron microscopy (HAADF-STEM) images of γ-CD-MOF@PTCA, which similarly demonstrate the cubic structure of γ-CD-MOF@PTCA. The elemental maps of the TEM show that C, O, and K are uniformly distributed in the material (Fig. 2f–h). X-ray powder diffraction (PXRD) of the composites showed that the materials retained the crystal structure of γ-CD-MOF after loading with PTCA, PDCA and PCA, respectively (Fig. 2i). As showed in Fig. 2j and S2, the Fourier transform infrared spectroscopy (FT-IR) absorption band at about 3400 cm^{-1} was attributed to the stretching vibration of –OH in γ-CD-MOF, whereas the stretching vibration peaks of –OH in γ-CD-MOF@PTCA, γ-CD-MOF@PDCA and γ-CD-MOF@PCA were not significantly shifted, indicating that the PTCA, PDCA, and PCA molecules did not interact with the hydroxyl groups of γ-CD-MOF. However, the absorption peaks of the attenuated total reflectance infrared spectra attributed to –OH of γ-CD-MOF@PTCA were shifted to some extent with increasing temperature, suggesting that the hydroxyl group may form a hydrogen bond with a small amount of water (Fig. S3a) [40,41]. The absorption peak near 1024 cm^{-1} was attributed to the stretching vibration of C—O—C in γ-CD-MOF [42], these results again demonstrated that the composites retained the original γ-CD-MOF structure. Interestingly, the weaker absorption peaks of –COOH and C═O attributed to PTCA and PDCA were observed at around 1690 cm^{-1} and 1762 cm^{-1}, whereas the presence of a stronger asymmetric stretching vibration peak attributed to COO^- at around 1593 cm^{-1} suggested the successful loading of PTCA, PDCA and PCA. This also suggests that the protons of the carboxyl group were captured by free hydroxide ions to form water molecules, and these water molecules further formed hydrogen bonds with COO^-, resulting in a larger proton conduction network [43,44]. The COO^- absorption peaks of the attenuated total reflectance infrared spectra of γ-CD-MOF@PTCA were slightly shifted with increasing temperature, again indicating the presence of hydrogen bonding (Fig. S3b). The perylene skeleton is a class of small molecules with high fluorescence quantum yields [45]. The emission spectra of γ-CD-MOF@PTCA are present at approximately 488 nm and 512 nm (excitation wavelength = 476 nm), which is attributed to the 0→0 (The higher energy peak for exciton recombination caused by the transition from the 0th vibrionic excited state to the 0th vibrionic ground state.) and 0→1 (The lower energy peak for exciton recombination caused by the transition from the 0th vibrionic excited state to the 1st vibrionic ground state.) [46] absorption bands in the π–π* electron transition (Fig. 2k). Franck-Condon values calculated on the basis of UV–vis spectroscopy provide evidence for the presence of PTCA as a monomer in the cavity of γ-CD [47–49]. For γ-CD-MOF@PTCA, the UV–vis spectra of PTCA have absorption peaks at 437 nm and 465 nm, those belong to the 0→0 and 0→1 absorption bands of the π-π* electron transition, respectively. PTCA exists in γ-CD-MOF as a monomer when Franck-Condon value $A_{\gamma-CD-MOF@PTCA}$ (i.e. $A_{0\rightarrow0}/A_{0\rightarrow1} = 1.02$) > 1. Similarly, for γ-CD-MOF@PDCA and γ-CD-MOF@PCA, PDCA and PCA exists in γ-CD-MOF as monomers (See S3 in supporting information for details). The above results suggests that PTCA, PDCA and PCA are present as monomers in the γ-CD cavity of γ-CD-MOF (Fig. S4), which is consistent with the previously reported barrel structure formation of perylene and γ-CD in a 1:2 ratio [50]. Furthermore, fluorescence calibration curves of PTCA, PDCA and PCA were obtained by fluorescence spectroscopy, respectively, from which the loading of PTCA, PDCA and PCA in the composites with different concentrations could be subsequently estimated (Fig. S5–S7, Table S1). In further investigation, the chemical compositions of the composites were characterized by X-ray photoelectron spectroscopy (XPS) (Fig. S8). In the C 1s spectrum and O 1s spectrum, the peak shift distances of C═O and C—O increased toward higher binding energy with the increase of carboxyl groups (γ-CD-MOF@PTCA > γ-CD-MOF@PDCA > γ-CD-MOF@PCA), which suggests that the higher number of carboxyl groups on the perylene molecule is favourable for the formation of hydrogen bond network [51–54]. Thus, the proton conductivity of artificial bionic ion channels can be regulated at the molecular level. Furthermore, as illustrated in Fig. S9a, the N_2 adsorption–desorption isotherms of γ-CD-MOF and γ-CD-MOF@PTCA demonstrate the presence of robust adsorption of N_2 at low relative pressure ($P/P_0 < 0.05$), indicating that they are type I adsorption isotherms and possess microporous structures. In addition, the BET surface area of the composites decreased from 623.4982 m^2/g to 495.3986 m^2/g after PTCA loading, and the pore size distribution remained 1–1.7 nm, which further indicated that the composites belonged to a microporous structure (Fig. S9b). As we know, when small molecule is loaded into the γ-CD-MOF, its nitrogen adsorption–desorption BET surface area decreases [40], so the above results of the experiment are consistent with this regularity. In conclusion, the decrease in the nitrogen adsorption–desorption isotherm is attributed to the occupation of the cavity of the γ-CD-MOF after loading PTCA.

3.2. Gas sensing performance

Firstly, effect of different molar ratios of γ-CD-MOF to PTCA on the CO_2 sensing performance was explored. The response value (R_g/R_0) of γ-CD-MOF toward 1000 ppm CO_2 was about 1.13. Upon the addition of a small quantity of PTCA, corresponding to a molar ratio of 48.97: 1 with respect to γ-CD-MOF, the response value increased to 1.76. The response value of the composites toward 1000 ppm CO_2 reached an optimum value of 2.88 when the molar ratio of γ-CD-MOF to PTCA was 15.71: 1. When the loading of PTCA was further increased, the sensitivity of γ-CD-MOF@PTCA toward 1000 ppm CO_2 decreased. This was attributed to the fact that the overloading of PTCA would lead to more competitive coordination of excess PTCA with K^+ happening, which would be adverse to the initially expected coordination of K^+ with the hydroxyl group on γ-cyclodextrins. And this competitive coordination consequently restricts the growth of γ-CD-MOF, resulting in the formation of a volume-limited hydrogen bond network and the reduction of CO_2 binding sites, and thus its CO_2 sensitivity decreases after PTCA is overloaded [55]. (Fig. 3a). Fig. 3b shows the resistance response and recovery curves of γ-CD-MOF@PTCA toward 1000 ppm CO_2. The response time and recovery time of γ-CD-MOF@PTCA are 265 s and 327 s, respectively. As shown in Fig. 3c, the γ-CD-MOF@PTCA exhibits stable response-recovery cycling curves toward 100, 500, and 1000 ppm CO_2. In addition, the material showed a segmented linear response to CO_2 from 1–5000 ppm (Fig. 3d and e). When the material is exposed to low concentrations of CO_2 (1–100 ppm), γ-CD-MOF@PTCA exhibits a higher sensitivity (0.00529 ppm^{-1}), which is attributed to the fact that the reactive sites on the surface of the material can completely capture small amounts of CO_2. At higher concentrations (100–5000 ppm), after occupying the surface sites of γ-CD-MOF@PTCA, the remaining CO_2 has

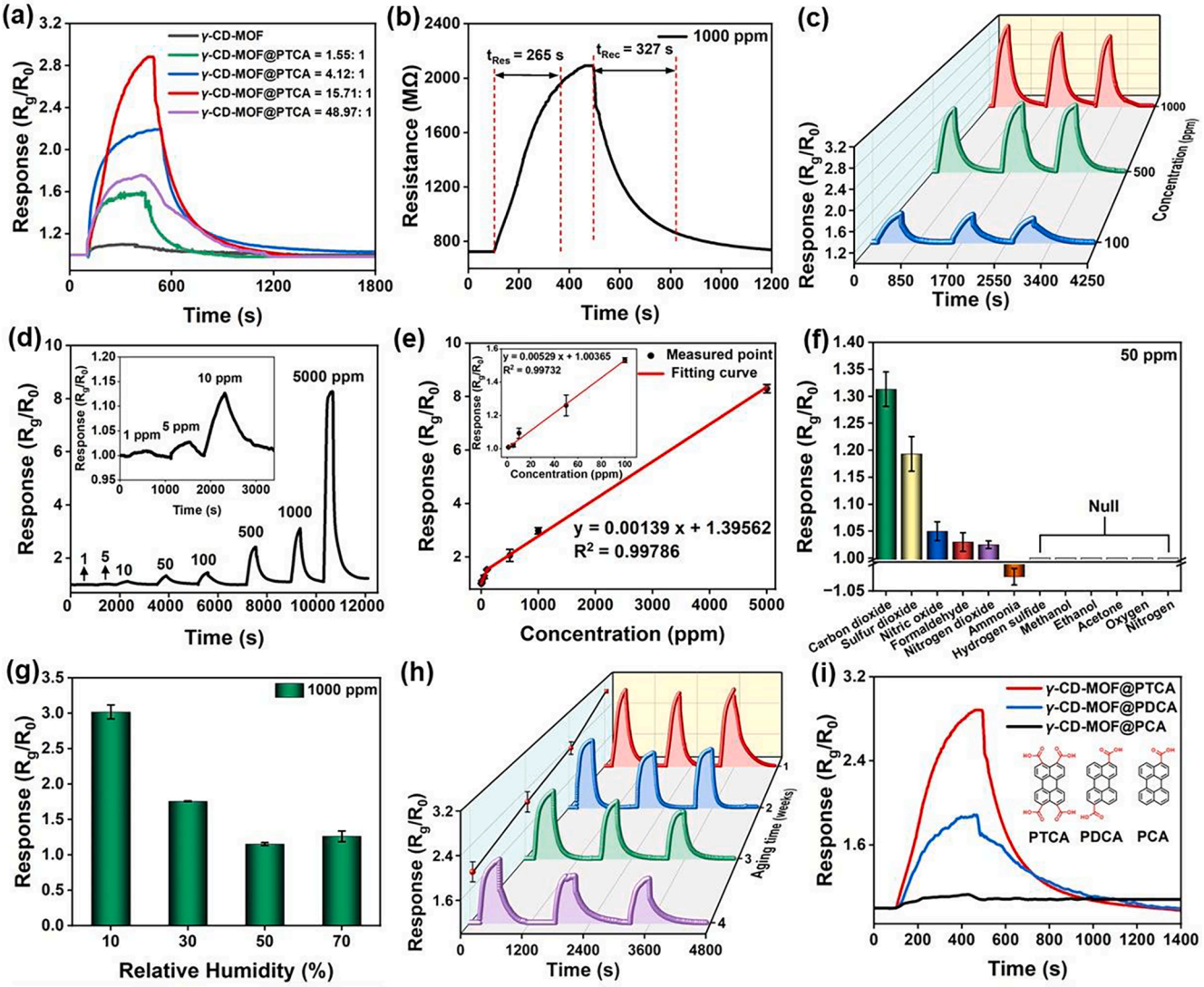

Fig. 3. Gas sensing performance. (a) Sensing performance of γ-CD-MOF@PTCA toward 1000 ppm CO_2 at different molar ratios. (b) Resistance response/recovery characteristics of γ-CD-MOF@PTCA before and after exposure to 1000 ppm CO_2 under RT. (c) Cycle curves of γ-CD-MOF@PTCA toward 100, 500, 1000 ppm CO_2. (d–e) Sensing performance and linear fitting curve of γ-CD-MOF@PTCA toward 1–1000 ppm CO_2. (f) The selectivity curve of the sensor toward 50 ppm CO_2 and various interfering gases, including 50 ppm SO_2, NO, NO_2, HCHO, NH_3, H_2S, CH_3OH, C_2H_5OH, CH_3OCH_3, O_2 and N_2. (g) Sensing performance of the sensor toward 1000 ppm CO_2 at a relative humidity of 10–70 % RH. (h) Long-term stability curve of γ-CD-MOF@PTCA. (i) Comparison of sensing performance of PTCA, PDCA and PCA with similar load in γ-CD-MOF toward 1000 ppm CO_2.

Table 1
Comparison of the performance of MOF-based chemiresistive CO_2 sensing materials.

Sensing Materials	Temperature (℃)	Sensing mechanism	CO_2 (ppm)	Response[a]	t_{res}/t_{rec} (s)
NH_2-UiO-66 (Zr) [20]	150	Lewis acid-base reaction	5000	1.13 $^{\varepsilon}$	about 50 /75
SnO_2@ZIF-67 [21]	205	Oxidation reaction	5000	1.20 $^{\varepsilon}$	about 30 /30
GA@UiO-66-NH_2 [22]	200	Lewis acid-base reaction	50,000	1.04 $^{\varepsilon}$	18 /18
MIL-53(Al)/CB (carbon black) [23]	R.T.	breathing effect of MIL-53	1,000,000	1.15 at 20 bar $^{\zeta}$	about 30
Zn-MOF-74 [24]	R.T.	Lewis acid-base reaction Proton conduction	1000	1.25 $^{\zeta}$	10800/10800
Co-MOF-74-TTF [25]	R.T.	Lewis acid-base reaction	1,000,000	/	200/–
Cu_3(HIB)$_2$ [26]	R.T.	Lewis acid-base reaction	1000	0.62 % (100 ppm)$^{-1}$ $^{\delta}$	420 /600
γ-CD-MOF-2 [27]	80 at recovery	Proton conduction	1,000,000	~550–fold	300 /2400
γ-CD-MOF-1 [28]	R.T.	Proton conduction	1,000,000	1/50 of the baseline	3 /10
γ-CD-MOF@RhB [35]	R.T.	H^+/OH^- ion conduction channel	10	1.02 $^{\zeta}$	157/487
			1000	2.24 $^{\zeta}$	
γ-CD-MOF@PTCA	**R.T.**	**H^+/HCO_3^- ion conduction channel**	**1**	**1.01** $^{\zeta}$	**265/327**
(This work)			**1000**	**2.88** $^{\zeta}$	

[a] For ease of comparison, the evaluation of response is converted as ε: Response = R_a/R_g, δ: Response = G/G_0 (G_0 = initial baseline current) and ζ: Response = R_g/R_0.

to diffuse into the internal pores of the γ-CD-MOF@PTCA, which makes the whole sensing process more complicated and time-consuming due to the bulky effect of the pores, and thus the sensitivity of γ-CD-MOF@PTCA is much lower (0.00139 ppm^{-1}) [56]. As expected, the of the γ-CD-MOF@PTCA show a much lower practical limit of detection (pLOD) of 1 ppm, which is 50 times lower than that of γ-CD-MOF, as the lowest one among the reported chemiresistive MOF-based CO_2 sensors so far (Table 1, Fig. S10). Subsequently, the selectivity of γ-CD-MOF@PTCA was verified (Fig. 3f). The results showed that the response of γ-CD-MOF@PTCA toward 50 ppm CO_2 was higher than that of other interfering gases at the same concentration, including sulfur dioxide (SO_2), nitric oxide (NO), nitrogen dioxide (NO_2), formaldehyde (HCHO), ammonia (NH_3), hydrogen sulfide (H_2S), methanol (CH_3OH), ethanol (C_2H_5OH), acetone (CH_3COCH_3), oxygen (O_2) and nitrogen (N_2).

Humidity resistance is an important index for gas sensing. γ-CD-MOF@PTCA showed good sensing performance for CO_2 at 10 % RH, and the sensing performance gradually decreased with the increase of humidity (30–70 % RH), which is attributed to the competitive reaction between water and CO_2 (Fig. 3g and S11). However, this problem can be solved by adding a pre-filter [57,58]. Fig. 3h shows that γ-CD-MOF@PTCA retains 75% of its sensing performance after aging for 3 weeks. PTCA consists of a perylene skeleton and four carboxyl groups, and the presence of the carboxyl groups should allow the construction of a larger hydrogen-bonding network with the hydroxide ions inside the γ-CD-MOF, which would enhance the proton conductivity and improve the CO_2 sensing performance. To verify this positive effect of PTCA, PDCA and PCA were also loaded into γ-CD-MOF for comparison. It should be noted that γ-CD-MOF@PTCA, γ-CD-MOF@PDCA, and γ-CD-MOF@PCA need to be at similar molar ratios for the comparison of CO_2 sensing performance, which can be estimated from the fluorescence spectra and fluorescence calibration curves of the perylene-containing skeleton small molecules and composites (Figs. S5–S7). As shown in Fig. 3i, the response value of γ-CD-MOF@PTCA toward 1000 ppm CO_2 was higher than that of the control (γ-CD-MOF@PTCA > γ-CD-MOF@PDCA > γ-CD-MOF@PCA) at similar molar ratio. In other words, the composite gas-sensitive response value gradually increases with the carboxyl groups content on the perylene skeleton (PTCA > PDCA > PCA). This is ascribed to the fact that the carboxyl groups form a larger hydrogen bond network with hydroxide ions on γ-CD-MOF, which is favourable for the enhancement of proton conduction and the improvement of CO_2 sensing performance. These results are consistent with the FT-IR and XPS.

3.3. Mechanism of Ion-Conduction and CO_2 sensing

Electrochemical tests were performed to verify the properties of the CO_2-switching-DIC. It is well known that γ-CD-MOF possesses both proton conductivity and CO_2 affinity because of the presence of hydroxyl groups. Wang et al. reported a bio-inspired CSPH ion-conducting channel material. After loading rhodamine B (RhB) into γ-CD-MOF, the amino group on RhB interacted with water molecules to generate a large number of hydroxide ions and thus constructed an artificial anion channel, which facilitated the detection of CO_2 at low concentrations and realized the controlled switching of H^+/OH^- ion channels [35]. Furthering this previous study, this work uses the carboxyl groups on the perylene skeleton to form a larger hydrogen bond network with the hydroxide ions within the γ-CD-MOF. As shown in Fig. 4a, the electromotive force (EMF) of γ-CD-MOF@PTCA is positive before CO_2 is injected into the test chamber, which means that the composite is dominated by proton conduction channels at this time, as evidenced by the XPS and FT-IR results (Fig. 2j and Fig. S6). When CO_2 was injected, CO_2 combined with free hydroxide ions within the γ-CD-MOF to form bicarbonate species, the hydrogen bond network was interrupted and proton conduction was limited, at which point bicarbonate can diffuse to

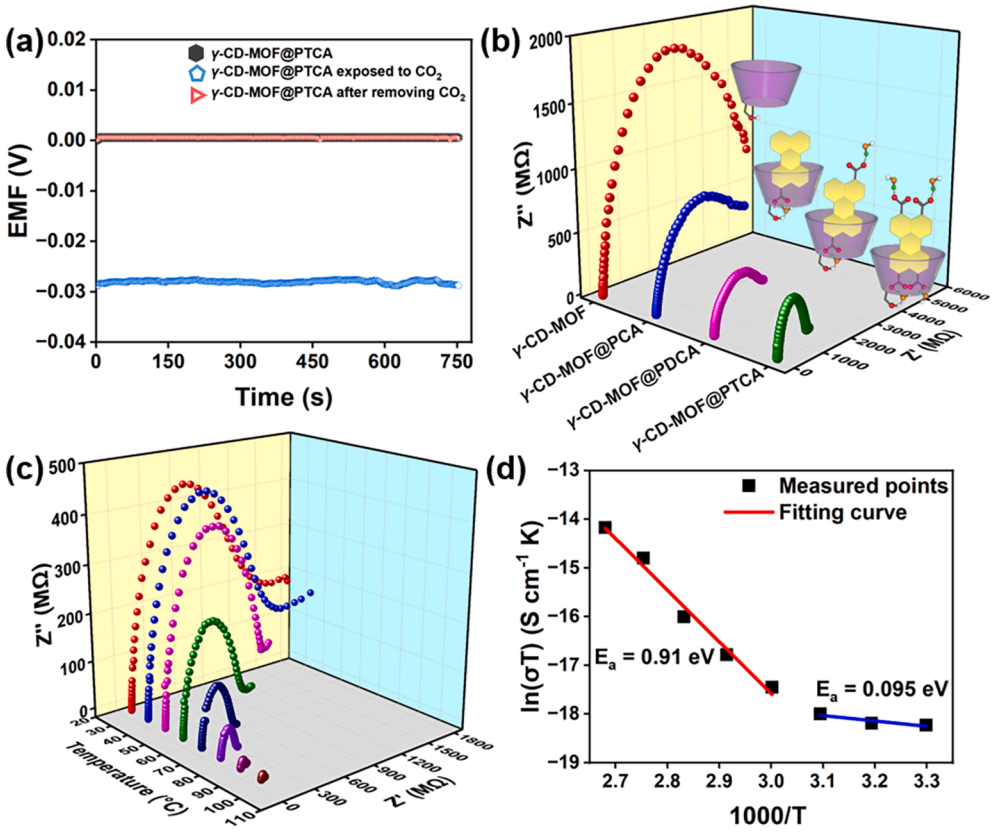

Fig. 4. Mechanism of ion-conduction. (a) Electromotive force plot of γ-CD-MOF@PTCA. (b) Comparison of impedance of γ-CD-MOF, γ-CD-MOF@PCA, γ-CD-MOF@PDCA and γ-CD-MOF@PTCA. (c) Nyquist plot of γ-CD-MOF@PTCA. (d) Arrhenius plot of γ-CD-MOF@PTCA.

some extent [59], and therefore the EMF became negative. After the removal of CO_2, the hydrogen bond network within γ-CD-MOF was restored. The extensive hydrogen bond network enabled the resurgence of proton conduction as the dominant mechanism, resulting in the EMF returning to a positive value. (Fig. 4a). These results demonstrated that γ-CD-MOF@PTCA is a CO_2-switched ion conduction/diffusion dual ion channel.

Fig. 4b and Table S7 present a comparative impedance analysis of the γ-CD-MOF, γ-CD-MOF@PCA, γ-CD-MOF@PDCA and γ-CD-MOF@PTCA. The results indicated that the resistance decreased with the further increase of carboxyl groups on perylene. According to the equation (1), the proton conductivity of the four materials can be calculated.

$$\sigma = l/RA \quad (1)$$

where l and A are the thickness and cross-sectional area of the tablet, and R is the resistance.

When PCA is loaded into the MOF, its proton conductivity increased by an order of magnitude over the pristine γ-CD-MOF, and the proton conductivity increased with the carboxyl group content ($\sigma_{\gamma-CD-MOF@PTCA} > \sigma_{\gamma-CD-MOF@PDCA} > \sigma_{\gamma-CD-MOF@PCA} > \sigma_{\gamma-CD-MOF}$). These results were consistent with the pattern of XPS and FT-IR, which imply that the hydrogen bond network of an artificial ion channel can be expanded or narrowed by modulating the content of functional groups to increase or decrease the proton conductivity of that artificial ion channel. Higher conductivity means that the proton hopping process is more active. Upon exposure to CO_2, the proton hopping process should be disrupted, resulting in a more significant change in resistance. Furthermore, the Nyquist plots of the composites demonstrated that the impedance of γ-CD-MOF@PTCA decreased with increasing temperature, indicating classical ion conduction properties (Fig. 4c). As shown in Fig. 4d, the Arrhenius plot of γ-CD-MOF@PTCA exhibited the segmented fitting curve. At 30–50 °C, the activation energy of γ-CD-MOF@PTCA was E_a = 0.0095 eV, indicating that the composite was a Grotthuss mechanism (i.e., proton hopping) at low temperatures ($E_a < 0.4$ eV). While at 60–100 °C, the activation energy for γ-CD-MOF@PTCA was E_a = 0.91 eV, implying that the composites follow the vehicle mechanism at higher temperatures ($E_a > 0.4$ eV).

A sensing mechanism based on artificial CO_2-switched ionic H^+ conduction/HCO_3^- diffusion ion channel was proposed according to the above results (Fig. 5). The protons on the carboxyl group of PTCA in the composite were captured by the hydroxide ions within the γ-CD-MOF and then formed hydrogen bonds, the protons hopping along this hydrogen bond network (Fig. 4c and d). When CO_2 is exposed to the composite, CO_2 can react with free hydroxide ions and a small amount of water in the test chamber to form bicarbonate ions and carbonic acid, respectively. In this process, the hydrogen bond network formed between PTCA and free hydroxide ions within the γ-CD-MOF is broken and proton conduction is restricted, when the conduction process were dominated by bicarbonate ions, resulting in a sharp increase in the resistance of the material. Upon the removal of CO_2, hydroxide ions are released, facilitating the reconstruction of hydrogen bond networks between PTCA and hydroxide ions. Consequently, proton conduction reassumes its dominant role. By such a cycle, a CO_2-controlled H^+ conduction/HCO_3^- diffusion ion channel was developed.

3.4. Detection of human exhaled CO_2

It is well known that the alveoli in the body produce large amounts of CO_2 during breathing, and lung abnormalities can lead to changes in the concentration of exhaled CO_2 in the body. For example, patients with chronic obstructive pulmonary disease (COPD) and COVID-19 have some degree of dyspnoea, which may lead to changes in the concentration of exhaled CO_2 [60,61]. It has been shown that CALU-1 lung cancer cell produce more CO_2 than the normal lung epithelial cells, NL20. [8] Therefore, non-invasive differentiation of healthy individuals from lung cancer patients based on the concentration of exhaled CO_2 is reasonable. In the present work, we measured and analysed the exhaled CO_2 of healthy individuals and lung cancer patients using γ-CD-MOF@PTCA sensing material, and all exhaled gas samples were obtained with the consent of the volunteers (Table S2–S4). All human breath samples were collected in an aluminium foil gas collection bag, and the collected gas had to be filtered of moisture by a simple filtration device before being injected into the test chamber prior to testing (Figs. S12–S14). First, exhaled breath samples from lung cancer patients aged 30–70 years were measured, and we observed no significant differences in exhaled CO_2 concentrations between lung cancer patients of different ages (Fig. S15). No significant differences in exhaled CO_2 concentrations were also observed in lung cancer patients of different genders (Fig. 6a). Notably, there is a clear distinction in the exhaled CO_2 concentrations between lung cancer patients and the healthy individuals, and the response-recovery curves for exhaled CO_2 concentrations in lung cancer patients are higher compared to those of healthy individuals (Fig. 6b). The mean concentration of exhaled CO_2 tested by γ-CD-MOF@PTCA in lung cancer patients was 1.98 times higher than in healthy volunteers (Fig. S16). To verify the accuracy of γ-CD-MOF@PTCA for exhaled CO_2 measurement, commercial IR meters were

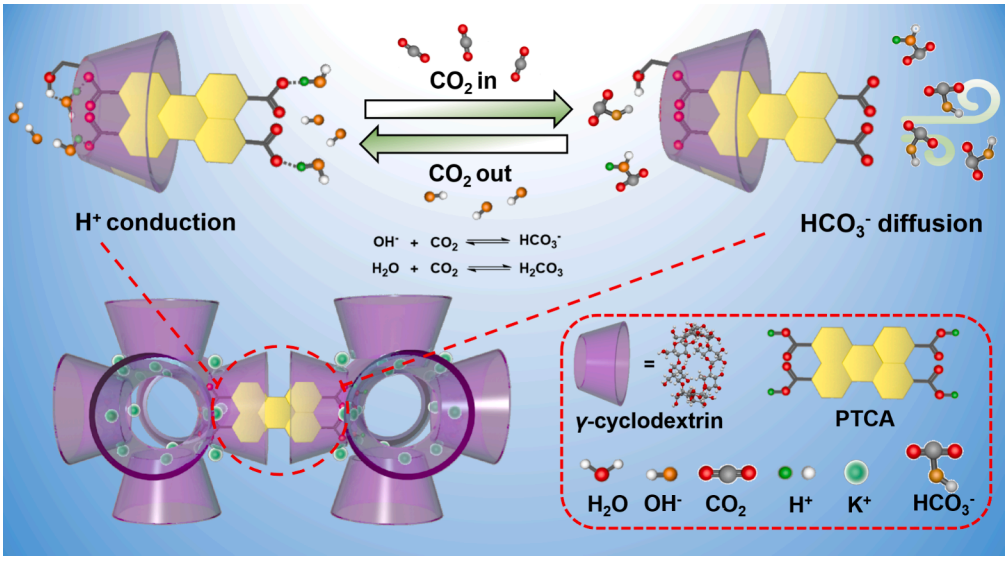

Fig. 5. Gas sensing mechanism of γ-CD-MOF@PTCA.

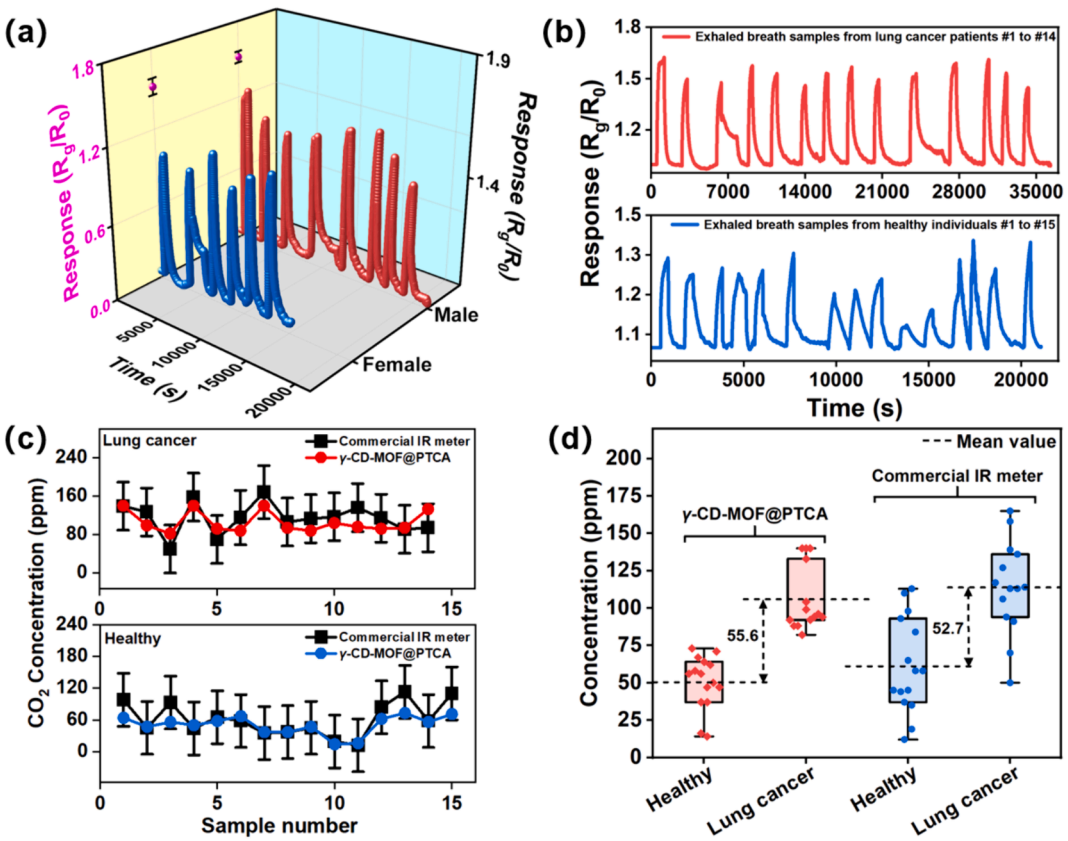

Fig. 6. Detection of human exhaled CO_2. Comparison of exhaled CO_2 concentrations in (a) male and female lung cancer patients. (b) healthy individuals and lung cancer patients. Comparison of (c) errors in exhaled CO_2 concentrations measured by γ-CD-MOF@PTCA and commercial IR meter, respectively. (d) exhaled CO_2 concentrations in healthy individuals and lung cancer patients using γ-CD-MOF@PTCA and commercial IR meter, respectively. Accuracy of differences is 94.5%.

also used for comparison. Tables S5 and S6 summarize the comparison of estimated CO_2 concentrations between healthy individuals and lung cancer patients after their exhaled breath was detected by γ-CD-MOF@PTCA and commercial IR meters, respectively. All the estimated CO_2 concentrations obtained by the γ-CD-MOF@PTCA test were within the margin of error of the commercial IR meter (Fig. 6c). More importantly, the difference between the mean concentrations of exhaled CO_2 in lung cancer patients and healthy individuals tested by the γ-CD-MOF@PTCA and commercial IR meters was 55.6 ppm and 52.7 ppm, respectively, with 94.5% accuracy between the two (Fig. 6d). The precise and pronounced differentiation observed indicates the significant potential of utilizing γ-CD-MOF@PTCA for detecting exhaled CO_2 as a non-invasive method for diagnosing lung cancer.

4. Conclusions

In summary, an artificial CO_2-switched H^+ conduction/HCO_3^- diffusion ion channel (CO_2-switching-DIC) was prepared. This CO_2-switching-DIC was used to prepare a room-temperature chemiresistive CO_2 sensor with high sensitivity, low pLOD, and good selectivity. The PTCA was loaded into the γ-CD cavity as a monomer, which modulated the hydrogen bond network of the material, and the bulky hydrogen bond network facilitated proton hopping, resulting in increased proton conductivity. The CO_2-switching-DIC generated a large amount of bicarbonate after the injection of CO_2 and then diffused, which is similar to the CO_2-induced opening of SLAC1 in stomatal defines cells during plant photosynthesis. The CO_2-switching-DIC sensor was also used to detect the CO_2 concentration in human exhalation and successfully discriminated between healthy individuals and lung cancer patients. This work not only deepened our understanding of artificial ion channels, but also created a non-invasive technique for detecting lung disease markers through exhalation.

Author contributions

H–H. C. and Y. W. conceived and designed the research; H–H. C. carried out the experiments; X–R.Y., Y–F. F., B. Z. and S–T. L. assisted the material preparation; Y–X. G., F–N. W., and H. L. helped conducting data analysis, Y–K. L. P–J. F., A–M.U.S., and G–F.Z. helped revising the manuscript; H–H. C. and Y. W. wrote the manuscript with input from all authors. All authors discussed, revised and approved the manuscript.

CRediT authorship contribution statement

Honghao Chen: Writing – review & editing, Writing – original draft, Visualization, Methodology, Investigation, Formal analysis, Data curation, Conceptualization. **Xiaorui Yue:** Investigation. **Yifei Fan:** Investigation. **Bin Zheng:** Investigation. **Sitao Lv:** Investigation. **Fengnan Wang:** Conceptualization. **Yixun Gao:** Validation. **Hao Li:** Conceptualization. **Yi-Kuen Lee:** Conceptualization. **Patrick J. French:** Conceptualization. **Ahmad M. Umar Siddiqui:** Conceptualization. **Yao Wang:** Writing – review & editing, Validation, Supervision, Resources, Funding acquisition, Conceptualization. **Guofu Zhou:** Conceptualization.

Declaration of competing interest

The authors declare that they have no known competing financial interests or personal relationships that could have appeared to influence the work reported in this paper.

Data availability

Data will be made available on request.

Acknowledgments

This work was supported by the National Natural Science Foundation of China, China (Grant No. 51973070); Science and Technology Program of Guangzhou, China (No. 2019050001); Guangdong Basic and Applied Basic Research Foundation, China (2022A1515010577, 2021A1515012420); Innovative Team Project of Education Bureau of Guangdong Province, China (2018KCXTD009); Guangdong Science and Technology Project–International Cooperation, China and the Netherlands (2022A0505050069); Startup Foundation from SCNU, China; Guangdong Provincial Key Laboratory of Optical Information Materials and Technology, China (2023B1212060065); MOE International Laboratory for Optical Information Technologies, China; the 111 Project, China; High–end Foreign Experts Recruitment Program, China (DL2023030001L).

Appendix A. Supplementary data

Supplementary data to this article can be found online at https://doi.org/10.1016/j.cej.2024.152633.

References

[1] T. DeVries, M. Holzer, F. Primeau, Recent increase in oceanic carbon uptake driven by weaker upper-ocean overturning, Nature 542 (2017) 215–218.
[2] A.P. Ballantyne, C.B. Alden, J.B. Miller, P.P. Tans, J.W.C. White, Increase in observed net carbon dioxide uptake by land and oceans during the past 50 years, Nature 488 (2012), 70–+.
[3] S.S. Myers, A. Zanobetti, I. Kloog, P. Huybers, A.D.B. Leakey, A.J. Bloom, E. Carlisle, L.H. Dietterich, G. Fitzgerald, T. Hasegawa, N.M. Holbrook, R.L. Nelson, M.J. Ottman, V. Raboy, H. Sakai, K.A. Sartor, J. Schwartz, S. Seneweera, M. Tausz, Y. Usui, Increasing CO_2 threatens human nutrition, Nature 510 (2014) 139–142.
[4] J.L. Scott, D.G. Kraemer, R.J. Keller, Occupational hazards of carbon dioxide exposure, J. Chem. Health. Saf. 16 (2009) 18–22.
[5] L. de Lary, A. Loschetter, O. Bouc, J. Rohmer, C.M. Oldenburg, Assessing health impacts of CO_2 leakage from a geological storage site into buildings: role of attenuation in the unsaturated zone and building foundation, Int. J. Greenh. Gas. Con. 9 (2012) 322–333.
[6] Y. Li, X. Wu, B. Yang, X. Zhang, H. Li, A. Umar, N.F. de Rooij, G. Zhou, Y. Wang, Synergy of CO_2 response and aggregation-induced emission in a block copolymer: a facile way to "see" cancer cells, ACS Appl. Mater. Inter. 11 (2019) 37077–37083.
[7] Y. Su, G. Chen, C. Chen, Q. Gong, G. Xie, M. Yao, H. Tai, Y. Jiang, J. Chen, Self-powered respiration monitoring enabled by a triboelectric nanogenerator, Adv. Mater. 33 (2021) 2101262.
[8] J. Sulé-Suso, A. Pysanenko, P. Španěl, D. Smith, Quantification of acetaldehyde and carbon dioxide in the headspace of malignant and non-malignant lung cellsin vitro by SIFT-MS, Analyst 134 (2009) 2419–2425.
[9] D. Crosby, S. Bhatia, K.M. Brindle, L.M. Coussens, C. Dive, M. Emberton, S. Esener, R.C. Fitzgerald, S.S. Gambhir, P. Kuhn, T.R. Rebbeck, S. Balasubramanian, Early detection of cancer, Science 375 (2022), 1244–+.
[10] S. Shai, F. Patolsky, H. Drori, E.J.J. Scheinman, E. Davidovits, G. Davidovits, S. Tirman, N. Arber, A. Katz, Y. Adir, A novel, accurate, and non-invasive liquid biopsy test to measure cellular immune responses as a tool to diagnose early-stage lung cancer: a clinical trials study, Resp. Res. 24 (2023).
[11] S. Xiao, Y. Yao, S. Liao, B. Xu, X. Li, Y. Zhang, L. Zhang, Q. Chen, H. Tang, Q. Song, M. Dong, Accurate and convenient lung cancer diagnosis through detection of extracellular vesicle membrane proteins via forster resonance energy transfer, Nano Lett. 23 (2023) 8115–8125.
[12] S. Moumen, I. Raible, A. Krauss, J. Woellenstein, Infrared investigation of CO_2 sorption by amine based materials for the development of a NDIR CO_2 sensor, Sensor. Actuat. B-Chem. 236 (2016) 1083–1090.
[13] M. Liu, R.M.M. Gray, L. Costa, C.R.R. Markus, A. Roy, A. Marandi, Mid-infrared cross-comb spectroscopy, Nat. Commun. 14 (2023).
[14] E. Tuetuencue, M. Nagele, S. Becker, M. Fischer, J. Koeth, C. Wolf, S. Kostler, V. Ribitsch, A. Teuber, M. Groeger, S. Kress, M. Wepler, U. Wachter, J. Vogt, P. Radermacher, B. Mizaikoff, Advanced photonic sensors based on interband cascade lasers for real-time mouse breath analysis, ACS Sens. 3 (2018) 1743–1749.
[15] B. Li, H. Wu, C. Feng, S. Jia, L. Dong, Noninvasive skin respiration (CO_2) measurement based on quartz- enhanced photoacoustic spectroscopy, Anal. Chem. 95 (2023) 6138–6144.
[16] C.A. Zito, T.M. Perfecto, A.-C. Dippel, D.P. Volanti, D. Koziej, Low-temperature carbon dioxide gas sensor based on yolk-shell ceria nanospheres, ACS Appl. Mater. Inter. 12 (2020) 17757–17763.
[17] A. Rossi, B. Fabbri, E. Spagnoli, A. Gaiardo, M. Valt, M. Ferroni, M. Ardit, S. Krik, A. Pedrielli, L. Vanzetti, V. Guidi, Functionalization of indium oxide for empowered detection of CO_2 over an extra-wide range of concentrations, ACS Appl. Mater. Inter. 15 (2023) 33732–33743.
[18] X. Li, K. Chen, R. Guo, Z. Wei, Ionic liquids functionalized MOFs for adsorption, Chem. Rev. 123 (2023) 10432–10467.
[19] M. Dinca, A. Iliescu, J.J. Oppenheim, C. Sun, Conceptual and practical aspects of metal-organic frameworks for solid-gas reactions, Chem. Rev. 123 (2023) 6197–6232.
[20] M.E. Dmello, N.G. Sundaram, A. Singh, A.K. Singh, S.B. Kalidindi, An amine functionalized zirconium metal-organic framework as an effective chemiresistive sensor for acidic gases, Chem. Commun. 55 (2019) 349–352.
[21] M.E. Dmello, N.G. Sundaram, S.B. Kalidindi, Assembly of ZIF-67 metal-organic framework over tin oxide nanoparticles for synergistic chemiresistive CO_2 gas sensing, Chem-Eur. J. 24 (2018) 9220–9223.
[22] K. Jayaramulu, M. Esclance Dmello, K. Kesavan, A. Schneemann, M. Otyepka, S. Kment, C. Narayana, S.B. Kalidindi, R.S. Varma, R. Zboril, R.A. Fischer, A multifunctional covalently linked graphene-MOF hybrid as an effective chemiresistive gas sensor, J. Mater. Chem. A 9 (2021) 17434–17441.
[23] P. Freund, L. Mielewczyk, M. Rauche, I. Senkovska, S. Ehrling, E. Brunner, S. Kaskel, MIL-53(Al)/carbon films for CO_2-sensing at high pressure, ACS Sustain. Chem. Eng. 7 (2019) 4012–4018.
[24] B. Ye, A. Gheorghe, R. van Hal, M. Zevenbergen, S. Tanase, CO_2 sensing under ambient conditions using metal-organic frameworks, Mol. Syst. Des. Eng. 5 (2020) 1071–1076.
[25] I. Strauss, A. Mundstock, M. Treger, K. Lange, S. Hwang, C. Chmelik, P. Rusch, N. C. Bigall, T. Pichler, H. Shiozawa, J. Caro, Metal-Organic framework Co-MOF-74-based host-guest composites for resistive gas sensing, ACS Appl. Mater. Inter. 11 (2019) 14175–14181.
[26] I. Stassen, J.-H. Dou, C. Hendon, M. Dinca, Chemiresistive sensing of ambient CO_2 by an autogenously hydrated Cu_3(hexaiminobenzene)$_2$ framework, ACS Cent. Sci. 5 (2019) 1425–1431.
[27] J.J. Gassensmith, J.Y. Kim, J.M. Holcroft, O.K. Farha, J.F. Stoddart, J.T. Hupp, N. C. Jeong, A metal-organic framework-based material for electrochemical sensing of carbon dioxide, J. Am. Chem. Soc. 136 (2014) 8277–8282.
[28] D. Shen, G. Wang, Z. Liu, P. Li, K. Cai, C. Cheng, Y. Shi, J.-M. Han, C.-W. Kung, X. Gong, Q.-H. Guo, H. Chen, A.C.H. Sue, Y.Y. Botros, A. Facchetti, O.K. Farha, T. J. Marks, J.F. Stoddart, Epitaxial growth of γ-cyclodextrin-containing metal-organic frameworks based on a host-guest strategy, J. Am. Chem. Soc. 140 (2018) 11402–11407.
[29] S. Thomine, H. Barbier-Brygoo, Structural biology a peep through anion channels, Nature 467 (2010) 1058–1059.
[30] Y.-H. Chen, L. Hu, M. Punta, R. Bruni, B. Hillerich, B. Kloss, B. Rost, J. Love, S. A. Siegelbaum, W.A. Hendrickson, Homologue structure of the SLAC1 anion channel for closing stomata in leaves, Nature 467 (2010) 1074–1157.
[31] J.-H. Kim, Y. Oh, H. Yoon, I. Hwang, Y.-S. Chang, Iron nanoparticle-induced activation of plasma membrane H^+-ATPase promotes stomatal opening in arabidopsis thaliana, Environ. Sci. Technol. 49 (2015) 1113–1119.
[32] M. Hashimoto-Sugimoto, T. Higaki, T. Yaeno, A. Nagami, M. Irie, M. Fujimi, M. Miyamoto, K. Akita, J. Negi, K. Shirasu, S. Hasezawa, K. Iba, A Munc13-like protein in Arabidopsis mediates H^+-ATPase translocation that is essential for stomatal responses, Nat. Commun. 4 (2013) 2215.
[33] K. Shimazaki, M. Iino, E. Zeiger, Blue light-dependent proton extrusion by guard-cell protoplasts by Vicia faba, Nature 319 (1986) 324–326.
[34] M. Zhang, Y. Wang, X. Chen, F. Xu, M. Ding, W. Ye, Y. Kawai, Y. Toda, Y. Hayashi, T. Suzuki, H. Zeng, L. Xiao, X. Xiao, J. Xu, S. Guo, F. Yan, Q. Shen, G. Xu, T. Kinoshita, Y. Zhu, Plasma membrane H^+-ATPase overexpression increases rice yield via simultaneous enhancement of nutrient uptake and photosynthesis, Nat. Commun. 12 (2021) 735.
[35] H. Chen, R. Lu, Y. Gao, X. Yue, H. Yang, H. Li, Y.-K. Lee, P.J. French, Y. Wang, G. Zhou, A bio-inspired and switchable H^+/OH^- ion-channel for room temperature exhaled CO_2 chemiresistive sensing, J. Mater. Chem. A 11 (2023) 21959–21971.
[36] Y. Chen, B. Yu, Y. Cui, S. Xu, J. Gong, Core-shell structured cyclodextrin metal-organic frameworks with hierarchical dye encapsulation for tunable light emission, Chem. Mater. 31 (2019) 1289–1295.
[37] L. Wang, X. Gao, Y. Wei, K. Liu, J. Huang, J. Wang, Y. Yan, Coordinating self-assembly of copper perylenetetracarboxylate nanorods: selectively lighting up normal cells around cancerous ones for better cancer diagnosis, ACS Appl. Mater. Inter. 10 (2018) 17630–17638.
[38] I. Roy, J.F. Stoddart, Cyclodextrin metal-organic frameworks and their applications, Acc. Chem. Res. 54 (2021) 1440–1453.
[39] L. Hu, K. Li, W. Shang, X. Zhu, M. Liu, Emerging cubic chirality in γCD-MOF for fabricating circularly polarized luminescent crystalline materials and the size effect, Angew. Chem. 59 (2020) 4953–4958.
[40] M. Peng, A.M. Kaczmarek, K. Van Hecke, Ratiometric thermometers based on rhodamine B and fluorescein dye-incorporated (nano) cyclodextrin metal-organic frameworks, ACS Appl. Mater. Inter. 14 (2022) 14367–14379.
[41] Y. Furukawa, T. Ishiwata, K. Sugikawa, K. Kokado, K. Sada, Nano- and microsized cubic gel particles from cyclodextrin metal-organic frameworks, Angew. Chem. 51 (2012) 10566–10569.
[42] F. Ke, M. Zhang, N. Qin, G. Zhao, J. Chu, X. Wan, Synergistic antioxidant activity and anticancer effect of green tea catechin stabilized on nanoscale cyclodextrin-based metal-organic frameworks, J. Mater. Sci. 54 (2019) 10420–10429.
[43] J.-R. Li, Y. Tao, Q. Yu, X.-H. Bu, Hydrogen-bonded supramolecular architectures of organic salts based on aromatic tetracarboxylic acids and amines, Cryst. Growth Des. 6 (2006) 2493–2500.

[44] H.-S. Zhang, X.-M. Dong, Z.-C. Zhang, Z.-P. Zhang, C.-Y. Ban, Z. Zhou, C. Song, S.-Q. Yan, Q. Xin, J.-Q. Liu, Y.-X. Li, W. Huang, Co-assembled perylene/graphene oxide photosensitive heterobilayer for efficient neuromorphics, Nat. Commun. 13 (2022) 4996.
[45] K. Hayashi, Y. Miyaoka, Y. Ohishi, T.-A. Uchida, M. Iwamura, K. Nozaki, M. Inouye, Observation of circularly polarized luminescence of the excimer from two perylene cores in the form of 4 rotaxane, Chem-Eur. J. 24 (2018) 14613–14616.
[46] B. Ghasemi, J. Ševčík, V. Nádaždy, K. Végsö, P. Šiffalovič, P. Urbánek, I. Kuřitka, thickness dependence of electronic structure and optical properties of F8BT thin films, Polymers 14 (2022) 641.
[47] S. Sowmiyha, V.V. Kumar, J. Pitchaimani, V. Madhu, R. Thiagarajan, N. S. Subramanian, S.P. Anthony, Self-assembly of water soluble perylene tetracarboxylic acid with metal cations: selective fluorescence sensing of Cu^{2+} and Pb^{2+} ions in paper strips, zebrafish and yeast, J. Lumin. 203 (2018) 42–49.
[48] A.K. Dwivedi, M. Pandeeswar, T. Govindaraju, Assembly modulation of PDI derivative as a supramolecular fluorescence switching probe for detection of cationic surfactant and metal ions in aqueous media, ACS Appl. Mater. Inter. 6 (2014) 21369–21379.
[49] F. Würthner, Z.J. Chen, V. Dehm, V. Stepanenko, One-dimensional luminescent nanoaggregates of perylene bisimides, Chem. Commun. 11 (2006) 1188–1190.
[50] G. Pistolis, A. Malliaris, Evidence for highly selective supramolecular formation between perylene/γ-CD and pyrene/γ-CD complexes in water, J. Phys. Chem. B 108 (2004) 2846–2850.
[51] F. Luan, Y. Wang, S. Zhang, X. Zhuang, C. Tian, X. Fu, L. Chen, Facile synthesis of a cyclodextrin-metal organic framework decorated with Ketjen Black and platinum nanoparticles and its application in the electrochemical detection of ofloxacin, Analyst 145 (2020) 1943–1949.
[52] Z.-J. Qiu, S.-T. Fan, C.-Y. Xing, M.-M. Song, Z.-J. Nie, L. Xu, S.-X. Zhang, L. Wang, S. Zhang, B.-J. Li, Facile fabrication of an AIE-active metal-organic framework for sensitive detection of explosives in liquid and solid phases, ACS Appl. Mater. Inter. 12 (2020) 55299–55307.
[53] S. Li, X. Hu, S. Chen, X. Wang, H. Shang, Y. Zhou, J. Dai, L. Xiao, W. Qin, Y. Liu, Synthesis of γ-cyclodextrin metal-organic framework as ethylene absorber for improving postharvest quality of kiwi fruit, Food Hydrocolloid. 136 (2023) 108294.
[54] W. Yuan, T. Ding, P. Mou, Y. Luo, L. Li, Y. Chen, X. Chen, J. Shu, L. Zhang, Semi-solid CNT@NaK anode for potassium metal battery, Adv. Funct. Mater. 33 (2023) 2209774.
[55] N. Sikdar, D. Dutta, R. Haldar, T. Ray, A. Hazra, A.J. Bhattacharyya, T.K. Maji, Coordination-driven fluorescent J-aggregates in a perylenetetracarboxylate-based MOF: permanent porosity and proton conductivity, J. Phys. Chem. C 120 (2016) 13622–13629.
[56] Y. Zhou, Y. Wang, Y. Wang, X. Li, Humidity-enabled ionic conductive trace carbon dioxide sensing of nitrogen-doped $Ti_3C_2T_x$ MXene/polyethyleneimine composite films decorated with reduced graphene oxide nanosheets, Anal. Chem. 92 (2020) 16033–16042.
[57] J. Wang, Y. Gao, F. Chen, L. Zhang, H. Li, N.F. de Rooij, A. Umar, Y.-K. Lee, P. J. French, B. Yang, G. Zho, Y. Wang, Assembly of core/shell nanospheres of amorphous hemin/ acetone-derived carbonized polymer with graphene nanosheets for room-temperature NO Sensing, ACS Appl. Mater. Inter. 14 (2022) 53193–53201.
[58] P.E. Silkoff, M. Carlson, T. Bourke, R. Katial, E. Ögren, S.J. Szefler, The Aerocrine exhaled nitric oxide monitoring system NIOX is cleared by the US Food and Drug Administration for monitoring therapy in asthma, J. Allergy Clin. Immun. 114 (2004) 1241–1256.
[59] Z. Yan, M. Zhang, F. Shi, B. Zhu, M. Liu, S. Wang, Y. Li, S.P. Nunes, Enhanced CO_2 separation in membranes with anion-cation dual pathways, J. CO_2 Util. 38 (2020) 355–365.
[60] C. Chang, C.-Y. Lee, N.-H. Tai, Human exhalation CO_2 sensor based on the PEI-PEG/ZnO/NUNCD/Si heterojunction electrode, ACS Omega 7 (2022) 15657–15665.
[61] C. Huang, L. Huang, Y. Wang, X. Li, L. Ren, X. Gu, L. Kang, L. Guo, M. Liu, X. Zhou, J. Luo, Z. Huang, S. Tu, Y. Zhao, L. Chen, D. Xu, Y. Li, C. Li, L. Peng, Y. Li, W. Xie, D. Cui, L. Shang, G. Fan, J. Xu, G. Wang, Y. Wang, J. Zhong, C. Wang, J. Wang, D. Zhang, B. Cao, RETRACTED: 6-month consequences of COVID-19 in patients discharged from hospital: a cohort study, Lancet 397 (2021) 220–232.